

Design of a horizontal neutron reflectometer for the European Spallation Source

D. Nekrassov^{a,e,*}, M. Trapp^{a,b}, K. Lieutenant^{a,e}, J.-F. Moulin^{c,e}, M. Strobl^d,
R. Steitz^{a,e}

^a*Helmholtz-Zentrum Berlin, Hahn-Meitner-Platz 1, D-14109 Berlin, Germany*

^b*Ruprecht-Karls-Universität, Im Neuenheimer Feld 253, 69120 Heidelberg, Germany*

^c*Helmholtz-Zentrum Geesthacht Outstation at Forschungs-Neutronenquelle Heinz
Maier-Leibnitz, 85747 Garching, Germany*

^d*European Spallation Source ESS AB, Box 176, 221 00 Lund, Sweden*

^e*German Work Package for the ESS Design Update*

Abstract

A design study of a horizontal neutron reflectometer adapted to the general baseline of the long pulse European Spallation Source (ESS) is presented. The instrument layout comprises solutions for the neutron guide, high-resolution pulse shaping and beam bending onto a sample surface being so far unique in the field of reflectometry. The length of this instrument is roughly 55 m, enabling $\delta\lambda/\lambda$ resolutions from 0.5% to 10%. The incident beam is focused in horizontal plane to boost measurements of sample sizes of $1 \times 1 \text{ cm}^2$ and smaller with potential beam deflection in both downward and upward direction. The range of neutron wavelengths utilized by the instrument is 2 to 7.1 (12.2, ...) Å, if every (second, ...) neutron source pulse is used. Angles of incidence can be set between 0° and 9° with a total accessible q -range from $4 \times 10^{-3} \text{ \AA}^{-1}$ up to 1 \AA^{-1} . The instrument operates both in θ/θ (free liquid surfaces) and $\theta/2\theta$ (solid/liquid, air/solid interfaces) geometry. The experimental setup will in particular enable direct studies on ultrathin films ($d \approx 10 \text{ \AA}$) and buried monolayers to multilayered structures of up to 3000 Å total thickness. The horizontal reflectometer will further foster investigations of hierarchical systems from nanometer to micrometer length scale (the latter by off-specular scattering), as well as their kinetics and dynamical properties, in particular under load (shear, pressure, external fields). Polarization and polarization analysis as well as the GISANS option are designed as potential modules to be implemented separately in the generic instrument layout. The instrument is highly flexible and offers a variety of different measurement modes. With respect to its mechanical components the instrument is exclusively based on current technology. Risks of failure for the chosen setup are minimum.

*Corresponding author

Email addresses: daniil.nekrassov@helmholtz-berlin.de (D. Nekrassov),
marcus.trapp@helmholtz-berlin.de (M. Trapp), klaus.lieutenant@helmholtz-berlin.de
(K. Lieutenant), jean-francois.moulin@hzg.de (J.-F. Moulin), markus.strobl@ess.se (M.
Strobl), roland.steitz@helmholtz-berlin.de (R. Steitz)

36 **1. Introduction and science case**

37 Soft matter and life science systems investigated by neutron reflectometry
38 (NR) continuously increase in complexity – both in structure as well as in the
39 number and the specific roles of their components. The same is true for hard
40 matter systems. This development presents a permanent challenge and demand
41 for continuous improvement of the neutron facilities. On the other hand there is
42 a constantly increasing request for NR measurements, in particular in soft mat-
43 ter and life sciences, which stems from the unique possibilities of neutrons in
44 probing amphiphilic and self-organizing structures at air-liquid [1, 2, 3], liquid-
45 liquid [4, 5] and solid-liquid (buried) interfaces [6, 7, 8, 9, 10]. NR in combination
46 with off-specular and grazing-incidence small angle neutron scattering (GISANS
47 [11], SESANS [12], SERGIS [13, 14, 15]) provides deep insight in self-assembly-
48 and aggregation processes [16], 1-3d ordered interfacial films [11, 17, 18, 19] and
49 the interplay of length scales in hierarchically structured systems [20].

50
51 Current research at the forefront of science with NR covers investigations
52 of protein organization in bio-membranes [21, 22], structure, organization and
53 functioning of living cells at interfaces [23], nano-engineering [24, 25, 26], new
54 materials and interface properties for energy (storage) applications [27, 28], mag-
55 netic fluctuations and domain propagation [29] as well as magnetic ordering and
56 the understanding of relevant length scales and energies [30].

57
58 Complementary (on-board) in-situ techniques in addition to NR are often
59 needed to elucidate complex interfacial structures and processes that are diffi-
60 cult to assess otherwise. In particular X-ray reflectometry [3, 31], ellipsometry
61 [32], Brewster angle microscopy [33, 34] and IR spectroscopy [34, 35, 36, 37, 38]
62 are essential complementary tools for achieving integrated insight into soft mat-
63 ter and life science systems. Soft matter sample sizes required by NR today are
64 typically of the order of 1000 mm² or larger which hinders studies with com-
65 ponents that are not available or cannot be produced in sufficient quantities.
66 The latter holds in particular, but not exclusively, for biological systems where
67 typically human proteins provide such bottle-neck. Thus, parametric studies for
68 instance on biological, genetic or pharmaceutical activity are outside the scope
69 of NR measurements today. Such investigations will become available with the
70 high flux of the ESS source by utilizing much reduced beam cross sections (foot
71 prints) and sample sizes.

72
73 Minimized beam dimensions (with not necessarily minimized sample size)
74 will further allow for characterizations of rough and curved interfaces that are
75 common in functional and natural materials like industrial coatings, ball bear-
76 ings, bone or skin. In addition, inhomogeneous, patterned surfaces might be
77 scanned for local features with sub-mm beams. Magnetic reference layers in
78 combination with polarized neutron beams offer additional contrast and sensi-
79 tivity for samples that do not withstand solution contrast changes [22]. In
80 combination with polarization analysis such experimental set-up will help dis-

81 crminating the incoherent background in soft matter and life science systems
82 by spin-filtering [39].

83
84 The ESS source [40] will enable kinetic studies of systems in non-equilibrium
85 situations on time scales not available today. Tackling the millisecond range in
86 the future however might still require concurrent sample sizes. Therefore, the
87 reflectometer at ESS should foresee flexible and adaptable collimation optics.
88 The latter is also important whenever interfaces are to be assessed from above
89 and below the sample horizon as can be the case for buried interfaces and inter-
90 faces under load, e.g. shear forces in combined NR and rheology set-ups [41, 42].

91
92 The length scale of interest in soft matter and life science systems of the
93 next generation will cover 1-3000 Å, hence an instrument with variable resolu-
94 tion from $0.5\% \leq dq/q \leq 10\%$ is required. For the majority of purposes (not
95 including wide angle and diffraction experiments) a q -range of 0.005 \AA^{-1} to 1
96 \AA^{-1} will suffice.

98 2. Layout of the horizontal reflectometer

99 The scientific motivation described in the last section combined with addi-
100 tional requirements from ESS advisory panels were taken into account when
101 choosing the basic instrument parameters. As a result, the key strength of this
102 instrument was decided to be the ability to use small samples and to access
103 large momentum transfer values q reaching up to $\approx 1 \text{ \AA}^{-1}$ in both downward
104 and upward direction for liquid samples. In order to match these requirements,
105 the following basic parameters were selected:

- 106 • Moderator: The horizontal reflectometer extracts neutrons from the cold
107 moderator providing the highest flux in the region of interest $\lambda \geq 2\text{ \AA}$.
- Instrument length L_{tot} : The instrument length is determined by the loos-
est desired resolution of $\delta\lambda/\lambda = 10\%$ and shortest design wavelength cur-
rently being 2 \AA . Based on the ESS pulse length of $\Delta t = 2.86 \text{ ms}$, L_{tot} is
calculated from:

$$\frac{\Delta t}{L_{\text{tot}}/v(\lambda = 2\text{ \AA})} = 10\%$$

108 which gives $L_{\text{tot}} = 56.6 \text{ m}$. The current length of the instrument design
109 is 54.9 m and thus very close to the analytical value.

- 110 • Usable waveband $\Delta\lambda$: Using the instrument length $L_{\text{tot}} = 54.9 \text{ m}$, the
111 pulse length $\Delta t = 2.86 \text{ ms}$ and the pulse frequency $f = 14 \text{ Hz}$, the width
112 of the waveband $\Delta\lambda$ before main frames start to overlap is: $\Delta\lambda = t_{\text{eff}} \times$
113 $v_0/L_{\text{tot}} = 5.1 \text{ \AA}$, where $t_{\text{eff}} = 1/f = 71.43 \text{ ms}$ and $v_0 = 3.956 \text{ m \AA/ms}$.
114 Thus wavelengths from 2 \AA to 7.1 \AA are used if every neutron pulse is
115 accepted. The width of the waveband can be increased to ≈ 12 (≈ 17 ,

116 ...) Å, if every second (third, ...) pulse is utilized. In principle, the used
117 waveband can be optimized for each measurement, by shifting it to lower
118 or higher wavelengths (e.g, 1.5 Å - 6.6 Å or 4 Å to 9.1 Å) to improve the
119 intrinsic resolution or q-range, respectively.

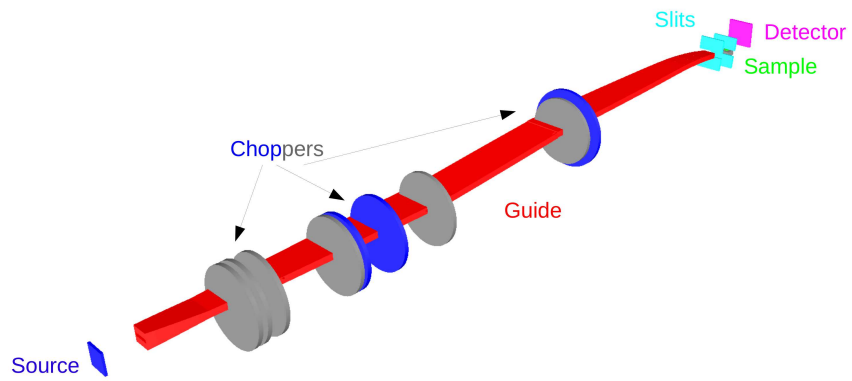
120 • Vertical guide shape: A horizontal reflectometer is to provide only a lim-
121 ited vertical divergence on the sample, which depends on the desired $\delta q/q$
122 resolution. Hence, a constant guide shape can be chosen in the vertical
123 plane, which does not provide large divergence on the sample and is easy
124 to build. At the same time, in order to achieve high q values of up to 1
125 Å⁻¹ in the case of free liquid surfaces, the beam needs to be bent onto
126 the sample surface by up to $\theta_i \approx 9^\circ$. Such a severe beam deflection is
127 very challenging and requires multiple reflections from tilted or curved
128 mirror surfaces, which is best managed with limited beam heights. Thus
129 the height of the beam h_0 is restricted to 2 cm. The beam deflection part
130 of the guide is described in the next section.

131 • Horizontal guide shape: It is expected that sample sizes for reflectometry
132 will tendentially decrease. To provide a sufficient neutron flux on samples
133 of the order of 1 cm², the guide system should have focusing properties
134 in the horizontal plane, hence the reflectometer is currently planned with
135 an elliptic guide [46, 47], starting with entrance/exit width of 10 cm and
136 a maximum width of 26 cm. The elliptic guide provides a focused beam
137 to either perform efficient measurements with small samples or restrict
138 the beam size to carry out position dependent studies. Still, the outgoing
139 beam is large enough for also addressing bigger samples, e.g. for time-
140 resolved measurements. The distance between the source and the guide
141 entrance is 2 m being currently the minimum distance, at which optical
142 components can be placed at the ESS. The first 4 m part of the guide is
143 thus inside the shielding monolith of 6 m radius and is referred to below
144 as the **extraction system** (guide part 1).

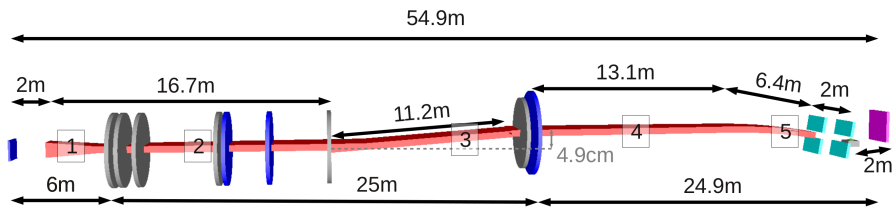
145 In the following, the layout of the instrument based on the key parameters
146 listed above is described in more detail (see also Tab. 1 for an overview). Indi-
147 vidual beamline components are presented and their characteristics are justified
148 based on results of neutronic MC simulations carried out with the VITESS
149 software package [44].

150 2.1. Moderator and extraction system

151 The reflectometer is set up for using wavelengths of 2 Å and longer. Based
152 on the current moderator description provided by the ESS and implemented in
153 simulation packages like VITESS [44] and McStas [45], the cold moderator with
154 12 cm edge length, which provides a larger flux for wavelengths longer than 2.5
155 Å, was selected for the reflectometer. Neutron optic elements can be placed
156 in the shielding monolith, which is currently 6 m in radius, beginning at 2 m
157 behind the moderator. Thus beamline components like mirrors or guides can



(a) Top view of the horizontal reflectometer



(b) Side view of the horizontal reflectometer

Figure 1: A sketch of the overall layout of the reflectometer. For positions and dimensions of individual components see Tab. 1. In the side view picture, different guide segments are denoted by numbers, see also Tab. 1. The choppers used in the basic setup are colored in blue, while the ones used for the WFM high-resolution setup are grey.

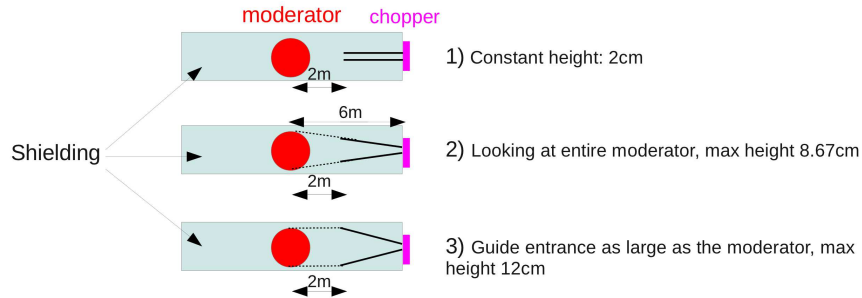


Figure 2: Sketch of the three options studied for the vertical geometry of the extraction system within the main shielding monolith.

158 be placed in the monolith to increase the number of neutrons fed into the main
 159 guide system outside the first 6 m. While the horizontal shape is elliptic (see
 160 above), three options were tested for the vertical shape of the extraction system,
 161 that is a constant height of 2 cm, and a tapered guide with the entry height of
 162 8.67 cm and 12 cm, respectively. For the latter, the guide entry height matches
 163 the size of the moderator. Simulations reveal that the best beam extraction is
 164 provided by the tapered feeding guide with 8.67 cm entry height, though it is
 165 noted that the performance of the constant guide is only slightly worse. The
 166 conclusion is that a large part of additional phase space accepted by the tapered
 167 guide is not transported by the subsequent beamline to the sample position.

168 2.2. Direct line of sight

169 A reflectometer aiming for high- q measurements needs to be free of prompt
 170 pulse background. Taking into account the unprecedented intensity of currently
 171 5 MW and the energy of the primary proton beam of ≈ 2.5 GeV it is unclear
 172 whether a T0-chopper is able to remove all of the fast particle and gamma-ray
 173 background. This is why a T0-chopper is not foreseen and the background from
 174 the prompt pulse is avoided by the geometry of the guide system. The latter
 175 has to be designed such that in the field of view of the detector, there are no
 176 guide elements that lie in the direct flight path from the source. This is the
 177 definition of **avoiding the line of sight twice**. Since the horizontal shape of the
 178 guide is elliptic and a modification of this shape would interfere with its
 179 focusing properties, avoiding the line of sight must be carried out in the vertical plane.

180
 181 As a sophisticated chopper system will be placed within the first few
 182 meters after the shielding monolith, where also one chopper needs to be moved
 183 along the beamline, it was decided to leave the in-monolith section horizon-
 184 tally, i.e. not to have any inclination in the guide system there. On the other
 185 hand, the guide section 4, which is upstream from the bending section, should
 186 be horizontal, to enable the latter to equally access samples from above and

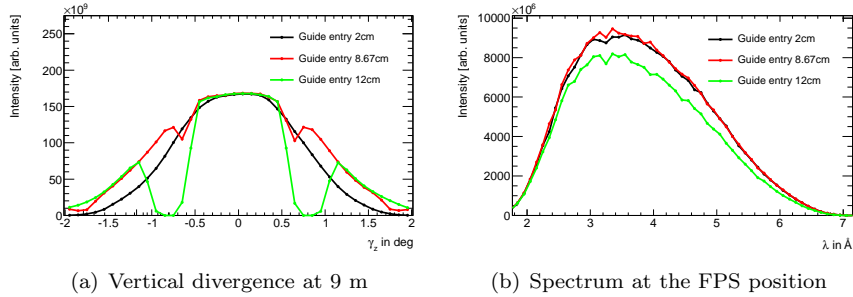
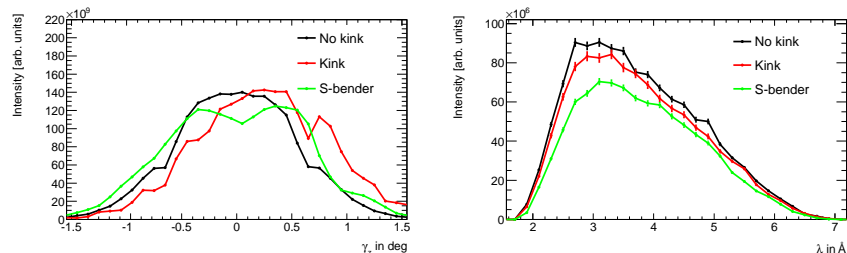


Figure 3: Performance comparison of three different solutions for the vertical shape of the extraction system. a) The vertical divergence distribution was measured 3 m downstream of the extraction system. The studied solutions show differences in the divergence distribution for $|\gamma_z| > 0.5^\circ$. b) The intensity as a function of wavelength was measured before the footprint slit at 52.9 m downstream of the moderator for a bending angle of 2° . The tapered guide option with 8.67 cm guide entry offers a slightly better performance than a constant height of 2 cm. The solution with the guide entry of 12 cm exhibits the worst performance of the three options studied.

187 below. Avoiding the line of sight requires a difference in height between the
 188 guide position at the monolith and at the bending section. Ways to achieve
 189 that are to place a double bender (**s-bender**) or a double kink (**z-kink**) in
 190 between. Here, a z-kink shows a clearly superior performance, see Fig. 4. The
 191 kink angle is fixed at $\alpha_K = 0.25^\circ$, which leads to very moderate losses only if
 192 compared with a guide system without a kink. The shift of the maximum in
 193 the vertical divergence distribution towards 0.25° can be reduced by optimizing
 194 the vertical shape of the kink guide element. The latter shows the best perform-
 195 ance if the shape is slightly double-elliptic. The total length of the kink guide
 196 section is 11.2 m and the shift in height of the guide position amounts to ≈ 5 cm.

197
 198 In accordance with the demand of avoiding the line of sight twice, the z-kink
 199 element should be placed such that fast primary particles are unable to illu-
 200 minate the guide section after the z-kink, independent of whether their flight
 201 path would interfere with the detector area. A simple raytracing study was per-
 202 formed to determine an optimal position of the latter guide element by scanning
 203 the neutron parameter space at the source between $-6 \text{ cm} \leq z_S \leq 6 \text{ cm}$ and
 204 $-2^\circ \leq \gamma_z \leq 2^\circ$, where z_S is the vertical coordinate of the neutron trajectory
 205 at the source and γ_z is its vertical divergence. The study revealed that if the
 206 z-kink is placed at a distance of 18.7 m away from the source, all fast particles
 207 would propagate at least 6 m outside the guide before entering the last guide
 208 section. Since propagation outside the guide can for simplicity be considered as
 209 propagation in shielding, it can safely be argued that due to the guide geometry,
 210 all fast background will be sufficiently absorbed and the prompt pulse will not
 211 contribute to the background at the detector position.

212



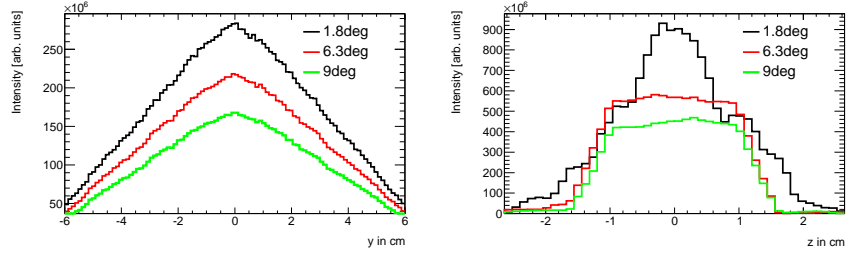
(a) Vertical divergence after leaving the line of sight (b) Spectrum at the sample position

Figure 4: (a) Comparison of the divergence distributions between instrument setups not avoiding the line of sight (no kink), or including an s-bender or z-kink mounted at 18.7 m downstream of the moderator. The z-kink option provides more flux (b) at the sample position due to a higher fraction of neutrons with low divergence after the z-kink, if compared with the S-bender option.

2.3. Beam delivery on sample

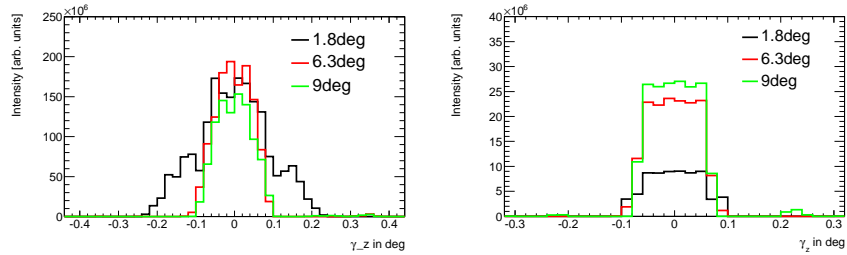
As stated above, in order to access a momentum transfer $q \approx 1 \text{ \AA}^{-1}$ on a free liquid surface the beam must have an incident angle on a horizontal sample of $\theta_{\text{tot}} \approx 9^\circ$, taking into account the shortest utilized wavelength of 2 \AA . Short wavelength neutrons require several bounces off the beam bending walls in order to be inclined by such large angle θ_{tot} , since there is a strong limitation on their maximum reflection angle, e.g. $\theta_{\text{max}} = 0.1m\lambda = 1^\circ$ for $m=5$ supermirror coatings. At the same time, the reflectometer is to provide sufficient flexibility concerning the variety of incident angles such that also regions of small $q \approx 0.005 \text{ \AA}^{-1}$ can be covered. Thus, the beam is tilted down- or upwards on a horizontal sample surface by means of 5 movable deflecting elements, of which the top and the bottom surfaces are covered with $m = 5$ coating. The length of each element is $\approx 1.28 \text{ m}$ with the height of 2 cm . When tilted by $\theta_i = 0.9^\circ$ each element bends the full beam of 2 cm height by 1.8° . The horizontal shape of the beam bending elements is elliptic, since these elements are still part of the main guide ellipse (see Fig. 1). The maximum bending angle $\theta_{\text{tot}} \approx 9^\circ$ guaranties for a maximum $q \approx 1 \text{ \AA}^{-1}$. Bending guide elements can be replaced upon request by a GISANS guide module providing horizontal collimation. The beam characteristics after the bending section are shown in Figs. 5 and 6. In principle, it is also possible to have shorter (1.15 m) bending elements that can be tilted by 1° , hence reaching the maximum reflection angle for a 2 \AA neutron. On the other hand, MC simulations show that in this case the intensity at wavelengths around 2 \AA is heavily suppressed.

The layout of the bending section is optimized for maximum flexibility and high- q while keeping the complexity of the system as low as possible. The five bending elements can be arranged to bend the neutron beam down- or upwards by a number of possible angles. Their work principle is that neutrons bounce



(a) Horizontal beam profile at footprint slit (b) Vertical beam profile at footprint slit

Figure 5: Beam profile measured perpendicular to the beam direction before footprint slit in horizontal and vertical direction for three different bending angles.



(a) Vertical beam divergence at footprint slit (b) Vertical beam divergence after footprint slit

Figure 6: Vertical divergence profile before footprint slit and at sample position for three different bending angles. The divergence profile before the footprint slit was measured perpendicular to the beam direction within $-1 \text{ cm} \leq y \leq 1 \text{ cm}$ and $-0.5 \text{ cm} \leq z \leq 0.5 \text{ cm}$. The first collimation slit was adjusted for an angular resolution $\delta\gamma_z/\gamma_z$ of 10%. The size of the second (footprint) slit matches the footprint of a $1 \times 1 \text{ cm}^2$ sample.

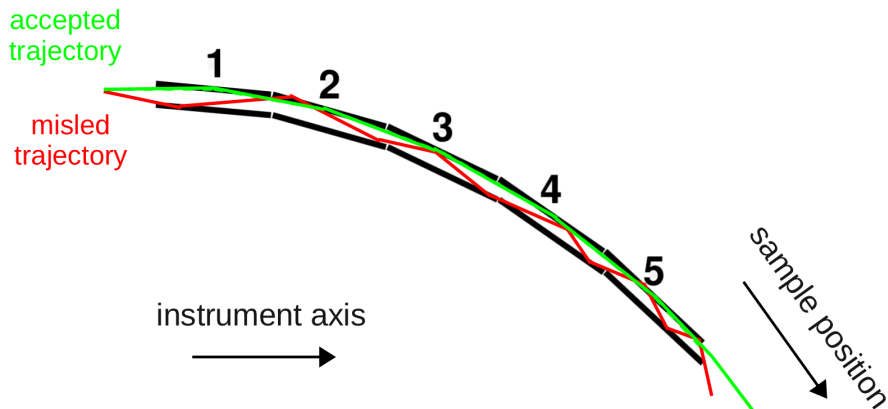


Figure 7: Illustration of the bending principle used in the reflectometer. The five bending elements are arranged such that by reflections off each of the element’s top (bottom) surface, the beam is deflected by the desired incident angle downwards (upwards) onto the sample. Neutrons with large divergence are likely to be deflected such that they either get absorbed or leave the bending section with even larger divergence, hence not propagating towards the sample.

241 off each element once and propagate towards the sample afterwards, see Fig.
 242 7. The drawback is that neutrons with a non-zero divergence have a certain
 243 chance of hitting the bottom (top) wall of one of the bending elements, if the
 244 beam is bent downwards (upwards). The resulting mis-orientation can be fur-
 245 ther increased during the propagation of the beam until the neutron is absorbed
 246 or leaves the bending section with a high divergence, i.e. does not propagate
 247 towards the sample. This is why the vertical divergence provided by the colli-
 248 mation system does not exceed 0.2° FWHM (0.3° as maximum) for higher
 249 bending angles, even though the maximum divergence can in principle achieve
 250 maximum $\approx 0.6^\circ$, taking into account the height of the guide of 2 cm and the
 251 collimation length of 2 m. It was investigated whether the divergence can be
 252 increased by involving more bending elements that would approximate a curved
 253 guide. This, however, would increase the mechanical complexity of the system,
 254 while MC simulations showed that there was no significant flux gain at the sam-
 255 ple position.

256

257 2.4. Collimation

258 The collimation of the neutron beam exiting the bending section of the guide
 259 is done by means of two diaphragms (slits) located at the guide exit and 2 m
 260 downstream from the guide, respectively. The first slit determines the total
 261 vertical divergence on the sample, while the second, so-called footprint slit, is
 262 used to reduce the beam size such that it matches the sample dimensions or
 263 the requirements for the beam size, e.g., for position sensitive measurements.

264 The adjusted divergence depends on the desired vertical angular resolution on
265 the sample. For simplicity one usually uses matching resolution for divergence
266 and wavelength, thus the opening (height) of the first slit depends on the pulse
267 shaping regime used. The free propagation length of 2 m further allows to in-
268 stall, e.g., a polarization device between the collimation slits.

269

270 *2.5. Pulse shaping*

271 The reflectometer operates with two chopper setups for basic and high-
272 resolution, respectively. All choppers are located at the side of the guide to
273 make use of the small beam height and thus reduce the opening/closing time.
274 The basic setup requires three choppers, which define the main frame and pre-
275 vent neutrons with other wavelengths from propagating to the detector. In
276 the basic setup, the wavelength resolution is defined by the total pulse length
277 $t_0 = 2.86$ ms. Hence the first chopper does not need to be close to the source,
278 as the pulse length will not be reduced. Furthermore, the first few meters after
279 the shielding monolith are occupied by pulse shaping choppers belonging to the
280 high-resolution setup (see below). Thus, the first chopper of the basic setup is
281 placed at 12.5 m, followed by a second chopper at 17.5 m and a third chopper
282 at 31 m. While the first two choppers are designed to suppress background
283 from slow neutrons that otherwise could pollute the subsequent frame(s), the
284 third chopper defines the accepted waveband of $2 - 7.1$ Å, if every source pulse
285 is used. The waveband can be extended, if every second (third) pulse is used,
286 see Fig. 8. This can be achieved by reducing the chopper rotation frequency to
287 $1/2$ ($1/3$, ...) of the original value.

288

289 A dedicated wavelength frame multiplication system (WFM) was developed
290 for the high-resolution work regime. Its purpose is to provide a high, constant
291 wavelength resolution between 0.5% and 2.2% for the utilized waveband, while
292 removing contaminant neutrons. This layout is very close to the one described
293 in [48] comprising six choppers in total. Solely the rotation speed of the first
294 three choppers is increased to 112 Hz to further reduce intensity losses, see Fig.
295 9 and Tab. 1. It is noted that the intensity loss in subframe overlap regions
296 is intrinsic to the way the WFM system is designed, as the subframes are kept
297 separated in time very strictly. This is necessary for highly structured reflec-
298 tivity spectra that are recorded with the high-resolution setup. In general, the
299 ansatz described in [49], which is very similar to the one used here, could lead
300 to less intensity losses in the subframe overlap regions, but at the expense of a
301 somewhat more challenging subframe separation.

302

303 *2.6. Sample environment*

304 In case of free liquid surfaces or situations where the interface of study needs
305 to be fixed in the horizontal plane, samples are put on a movable sample table
306 equipped with motors for necessary movements in horizontal and in vertical

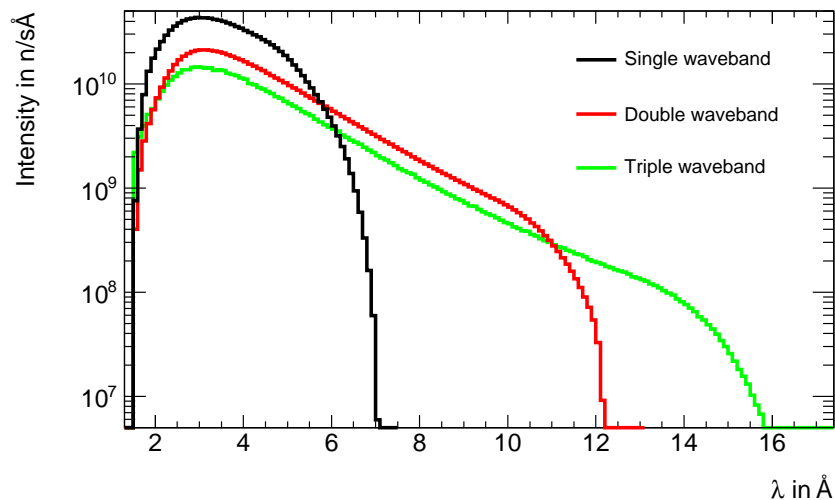


Figure 8: The neutron spectrum as provided by the basic chopper layout of the reflectometer measured after the third chopper. By adjusting the rotation speed of the choppers the reflectometer can be provided with a single (double, ...) waveband ending from 2 Å to 7.1 (≈ 12 Å, ...). Since only every second (third) pulse is used to extract the double (triple) waveband, for neutron wavelengths contained in the single waveband the flux is consequently reduced.

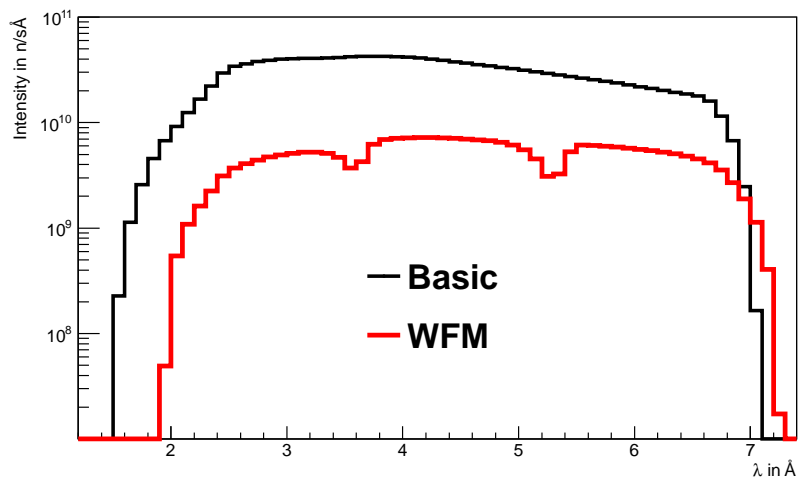


Figure 9: Comparison between the neutron fluxes in front of Slit 1 (see Tab. 1 for position) using the basic and high-resolution setup, adjusted for a 1% $\delta\lambda/\lambda$ resolution, for a reflection angle of 1.5° . The intensity drop in the spectrum of the high-resolution system arises from strict prevention of subframe overlap at the detector position.

307 direction. The positional displacement of the sample from the z_0 position of
308 the main guide (upstream the bending section) is 84 cm at maximum for the
309 highest possible deflection angle of 9° . This maximum vertical movement is only
310 1.7 times the vertical displacement of the sample stage realized at FIGARO at
311 present and thus, will not pose any difficulty in handling on the instrument.
312 The sample table will allow for accessing the sample by the neutron beam from
313 above and below. In the case of air-solid and solid-liquid interfaces samples will
314 be tilted against the fixed incident beam in the horizontal at fixed zero height
315 thus operating the instrument in the more simple $\theta/2\theta$ mode. In addition,
316 there should exist enough space for sample environment controlling temperature,
317 pressure, mechanical load etc. For the very reason the distance between the
318 sample position and the footprint slit is set to 40 cm.

319 *2.7. Detector*

320 It is envisaged that the reflectometer comprises a position sensitive area
321 detector of $50 \times 50 \text{ cm}^2$, located 2 m away from the sample position, with a
322 pixel size fine enough to match the angular resolution. The smallest reflection
323 angles are expected to be $0.3^\circ - 0.4^\circ$. Taking into account the loosest
324 wavelength resolution of 10% the detector resolution should be $\approx 0.03^\circ$. Using
325 $\Delta h/2 = \tan(\Delta\gamma_0^\circ) \times 2 \text{ m} \approx 1 \text{ mm}$, where Δh is the pixel size and $\Delta\gamma_0 = 0.03^\circ$
326 the desired resolution expressed in σ under the presumption that the divergence
327 distribution is Gaussian, it follows that a detector with pixels having 2
328 mm edge length fulfills the instrument requirements. Furthermore, it will be
329 advantageous that the detection process takes place in a single conversion layer,
330 since in this case the detector can be tilted by an angle α_{det} w.r.t the neutron
331 flight path after the sample to improve the angular resolution in vertical
332 direction to $\Delta\gamma(\alpha_{\text{det}}) = \Delta\gamma_0 \cos(\alpha_{\text{det}})$. Such setup could even match the high
333 wavelength resolution achieved with the WFM chopper setup.

334

335 *2.8. SERGIS add-on*

336 As mentioned in the Introduction, interfacial systems continuously increase
337 in complexity. While in the last decade main focus of neutron scattering investigations
338 of interfaces was on 1-dimensional systems, this will change in near future with the
339 development of hierarchical 2D- to 3D-ordered systems on nanoscale. Typical examples
340 are porous interfacial films for use in catalysis, as scaffolds or templates for nanomaterial
341 synthesis [24, 25, 26], as selective cell culture substrates [23], separation media, energy
342 storage materials [27, 28], spin valves or magnetic random access memory devices [29].
343 This development requires continuous improvement of adequate instrumentation for analysis.
344 Here, SERGIS (Spin-Echo Resolved Grazing Incidence Scattering) [50, 51] as add-on
345 offers a promising route for the investigations of 2-3D structures on nanoscale.
346 It utilizes the polarized beam of the instrument, can be mounted without alterations
347 of instrument length into the reflectometry set-up and decouples the intensity of the
348 incident beam from the resolution of the experiment. Although
349

Component	Position [m]	Characteristics, parameters
Moderators		
Cold moderator	0	Liquid para-hydrogen, peak intensity at ≈ 2.5 Å
Basic guide characteristics		
Guide	2	Length: 48.5 m, Horizontal shape: elliptic with $W_i = W_f = 10$ cm, W_{\max} : 26 cm, m=3 coating, moderator and footprint slit at focal points Vertical shape: variable, m=5 coating
Guide part 1 (Extraction system)	2	$L = 4$ m, $W_i = 10$ cm, $W_f = 16.6$ cm, $H_i = 8.67$ cm, $H_f = 2$ cm, linear shape
Guide part 2	6	$L = 12.7$ m, $W_i = 16$ cm, $W_f = 25.0$ cm, $H_i = H_f = 2$ cm, vertical shape constant
Guide part 3 (z-kink)	18.7	$L = 11.2$ m, $W_i = 25.0$ cm, $W_f = 25.9$ cm, $H_i = H_f = 2$ cm, vertical shape double elliptic, $H_{\max} = 2.6$ cm, $H_{1/2L} = 2$ cm
Guide part 4	29.9	$L = 14.2$ m, $W_i = 25.9$ cm, $W_f = 19.1$ cm, $H_i = H_f = 2$ cm, vertical shape constant
Guide part 5 (bending section)	44.1	$L = 6.4$ m, composed of 5 tiltable sections of $L_s = 1.28$ m $W_i = 25.0$ cm, $W_f = 25.9$ cm $H_i = H_f = 2$ cm, vertical shape constant
Choppers		
Basic setup		
Basic chopper 1	12.5 m	$\omega = 14$ Hz, $R = 40$ cm, $W_i, f = 22$ cm
Basic chopper 2	17.5 m	$\omega = 14$ Hz, $R = 40$ cm, $W_i, f = 25$ cm
Basic chopper 3	31 m	$\omega = 14$ Hz, $R = 40$ cm, $W_i, f = 26$ cm
WFM setup		
Pulse shaping chopper 1	6	$\omega = 112$ Hz, $R = 35$ cm, $W_i, f = 17$ cm
Pulse shaping chopper 2	6.25 m – 7.08 m	$\omega = 112$ Hz, $R = 35$ cm, $W_i, f = 17 - 18$ cm
Frame overlap chopper 1	7.5	$\omega = 112$ Hz, $R = 35$ cm, $W_i, f = 18$ cm
Frame overlap chopper 2	12	$\omega = 56$ Hz, $R = 40$ cm, $W_i, f = 22$ cm
Frame overlap chopper 3	19	$\omega = 28$ Hz, $R = 40$ cm, $W_i, f = 25$ cm
Frame overlap chopper 4	30.4	$\omega = 14$ Hz, $R = 40$ cm, $W_i, f = 26$ cm
Collimation system		
Slit 1	50.5	$W = 10$ cm, height depends on required divergence
Slit 2	52.5	Width and height depend on sample size and incident angle
Sample table	52.9	Space for sample environment: 40 cm
Detector	54.9	Position-sensitive pixel detector $W \times H = 50 \times 50$ cm ² , pixel size 2 mm

Table 1: Instrument components and their parameters used in the design of the reflectometer. Used symbols: Guide entry/exit width W_i/W_f (also at chopper positions); Guide entry/exit height H_i/H_f ; Maximum guide width/height W_{\max}/H_{\max} ; Component length L ; Angular chopper speed ω ; Chopper radius R ; Detector width/height W/H . See text for further details.

350 SERGIS is still not matured, in particular with respect to data interpretation
351 and analysis [52, 53], there is a great potential of this technique. In particular
352 when used as rather simple **add-on**, and limited to nanoscale, functional sys-
353 tems, both in soft matter and life sciences [15] as well as in materials science
354 [14], also under non-equilibrium conditions might be explored with high spatial
355 and temporal resolution.

356 The design of the SERGIS add-on is developed to fit the conditions imposed
357 by the layout of the liquids reflectometer. For the setup 2 m in front and be-
358 hind the sample position are available. Figure 10 shows the technical design of
359 the complete setup (polariser and analyser not shown). The installation at the
360 incoming (upstream) side accommodates

- 361 1. polariser (S-bender or polarized ^3He gas cell), which is able to polarise a
362 polychromatic beam with high efficiency.
- 363 2. adiabatic gradient field radio frequency spin flipper for calibration and
364 measurement possibility with both polarisations (spin up and spin down)
- 365 3. gradient-field coupling device (Forte coil) between the low field region
366 (spin-echo precession devices, i.e. magnetic air-core coils with relatively
367 weak fields) and the strong field region of the analyser
- 368 4. first pair of triangular coils (A)
- 369 5. guide field (GF1)
- 370 6. second pair of triangular coils (B)

371 The setup behind the sample (downstream) consists of:

- 372 1. third pair of triangular coils (C)
- 373 2. guide field (GF2)
- 374 3. fourth pair of triangular coils (D)
- 375 4. gradient-field coupling device (Forte coil, (FC)) between the strong-field
376 region (polarizer, flipper with strong permanent magnets) and the low-
377 field region (spin-echo precession devices, i.e. magnetic air-core coils with
378 relatively weak fields)
- 379 5. analyser (multi-cavity) (Ana)
- 380 6. position sensitive 2D detector (PSD)

381 The guide field (GF1,2) is 1m in length in order to leave enough room on the
382 incoming side to accommodate all spin manipulation devices. The angle χ of
383 the triangular coils with respect to the incoming neutron beam can be changed
384 between 30° and 60° depending on the orientation of the coils (see Figure 10).
385 Magnetic fields used lie in the range from 1.5 to 15 mT. Above parameters in
386 combination with a wavelength band of 2 - 7.1\AA (2 - 12° , every second pulse)
387 result in a spin echo length of 5-662 nm (30°) and 9-1150 nm (5-1850 nm, 30°
388 and 90-3200 nm, 60°).

389 2.9. GISANS add-on

390 The alternative module for studies of laterally structured interfacial systems
391 is a GISANS add-on. For this reason the reflectometer can also be equipped

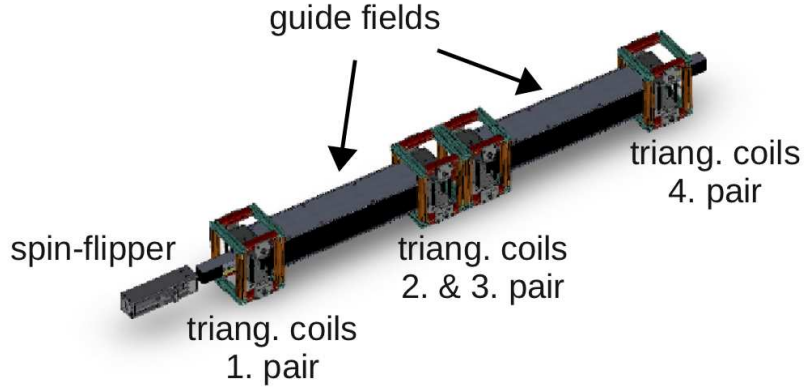


Figure 10: Schematic representation of the SERGIS add-on. Shown are polariser, spin-flipper, triangular coils and guide fields.

392 with a conventional GISANS module. The collimation concept of this module is
 393 based on the approach successfully used at REFSANS [43]. In this concept the
 394 sample is illuminated by multiple low divergence beams which all converge to a
 395 single focus point on the detector (Fig. 11). In this way the best possible use of
 396 the available source divergence is realized and a high reciprocal space resolution
 397 is maintained. The radial collimator is replacing guide part 5 (bending section)
 398 and the collimation slits in front of the sample (see Fig. 1 (b) and Tab. 1).
 399 It consists of elements with non-reflecting side walls. Top and bottom walls
 400 are made from $m=5$ mirrors in order to provide sufficient beam bending for
 401 GISANS experiments. The collimator is divided laterally in three sub-channels
 402 separated by 0.1 mm thick absorbing walls. The chosen length L of the colli-
 403 mator is 6.4m with $w_1 = 5$ mm and $w_2 = 3.3$ mm. The detector is placed at
 404 5.7 m downstream from the collimator exit with a sample-to-detector distance,
 405 LSD, of 5 m, slightly reducing the usable waveband by $\approx 5\%$. In the chosen 3
 406 beams configuration, the intensity distribution is homogeneous horizontally (see
 407 Fig. 12). The shadows of the collimator walls are small in comparison to the
 408 individual beam width. This ensures a very good sample illumination ($> 90\%$).
 409 From Fig. 13 a) it appears that all three channels deliver the same intensity
 410 (resp. 30%, 38%, 32% of the total), which ensures a homogeneous sampling of
 411 the surface.

412

413 The long collimation distance produces an intensity distribution that is uni-
 414 form over the total horizontal divergence (Fig. 13, left panel), and does not
 415 exceed ± 1 mrad. As expected, each of the beams contributes equally to this
 416 divergence (Fig. 13, middle panel). At the detector position, which was chosen

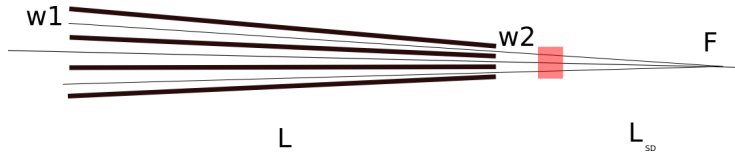


Figure 11: Schematics of the radial collimator with L = collimation length, LSD = sample-to-detector distance, F = focal point, $w1$, $w2$ = width of collimator channels at entrance, exit of the collimator.

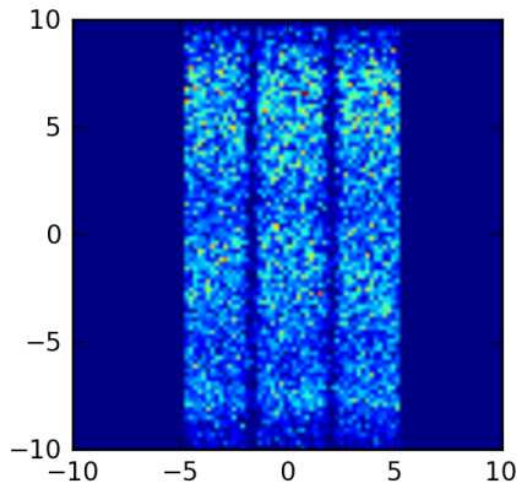


Figure 12: Illustration of expected 2D intensity distribution at the collimator exit.

417 to be 5 m from the sample in order not to depart too much from the normal
 418 operation distance of the reflectometer, one observes -as desired- a single spot
 419 of 4 mm full width at half maximum, matching the targeted in-plane resolution
 420 (Fig. 13, right panel). In conclusion the radial collimation option offers the
 421 possibility to perform GISANS measurements at the liquid reflectometer with
 422 a resolution matching that of a current state-of-the-art SANS instrument.

423 3. Performance

424 The layout of the horizontal reflectometer is optimized for measurements
 425 with small samples and high q transfers. Its performance is demonstrated by
 426 carrying out virtual experiments with different samples of $1 \times 1 \text{ cm}^2$ area. Fluxes
 427 and count rates are given for different angular and resolution settings, which
 428 are summarized in Tab. 2. The beam intensity at the sample position is also

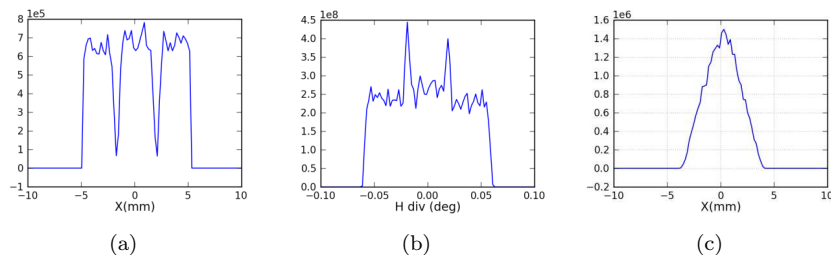


Figure 13: Illustration of expected (a) intensity distribution in the horizontal plane at collimator exit, (b) horizontal divergence (full beam) at sample position, (c) profile of the beam at the detector position. The intensity is in arbitrary units.

429 shown for selected angular settings in Fig. 14. The simulations were carried out
 430 including the ESS cold moderator characteristics as of May 2013.

431 3.1. Basic setup

432 As discussed in the previous section, the basic setup of the reflectometer
 433 utilizes three choppers that provide the desired waveband with the wavelength
 434 resolution mainly determined by the length of the instrument going up to 10%
 435 for 2 Å neutrons. The slit collimation yields a vertical beam divergence that
 436 matches the loosest wavelength resolution (but is restricted to max. $\approx 0.6^\circ$
 437 FWHM). Such a setup is most suitable for measuring reflectivity spectra of free
 438 liquid surfaces and monolayers on liquid surfaces, like e.g. Langmuir and Gibbs
 439 adsorption layer of amphiphiles. The measurement can be performed using the
 440 single waveband and three angular settings or the double waveband and two
 441 angular settings (and so on). In general, for each angular setting the waveband
 442 can be freely selected, e.g. for small angles it is advantageous to use a larger
 443 waveband, since the reflectivity is high at low q and thus a larger q -region can
 444 be covered with a measurement time still being of the order of a few seconds.
 445 The applicability will depend on the time required by the choppers to change
 446 settings from single to double (triple,...) waveband regime.

447
 448 The measured reflectivity curves of an ideal D₂O reflectivity surface and an
 449 adsorption monolayer¹ and corresponding count rates are shown in Fig. 15.
 450 The usage of the double waveband leads to a larger measurement time, but on
 451 the other hand the time needed to adjust for an intermediate reflection angle
 452 is saved. The longest measurement time is required, as expected, for high-
 453 est angular settings. Nevertheless, it is possible to measure reflectivities up to

¹The free floating Langmuir layer is a condensed monolayer of 1,2-dipalmitoyl(d62)-sn-glycero-3-phosphoethanolamine (d-DPPE), chosen as a reference monolayer of amphiphilic molecules. The d-DPPE layer is 23 Å thick, has an SLD of $5.63 \times 10^{-6} \text{ \AA}^{-2}$ and comes with rms roughness of 2 Å at both the headgroup/liquid and the tailgroup/air interface. The parameters of the d-DPPE Langmuir layer are based on x-ray data [54, 55, 56].

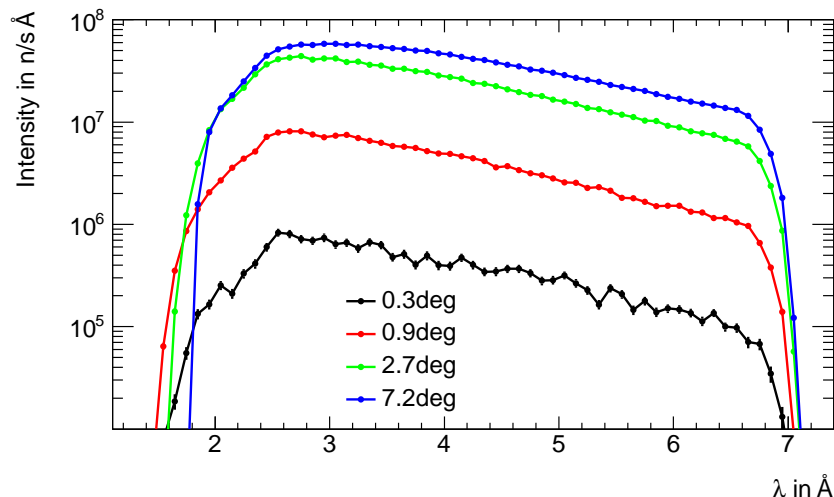
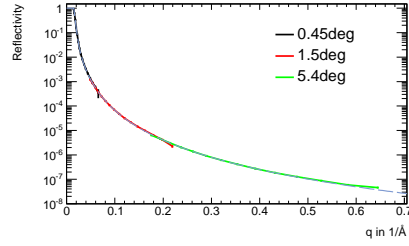


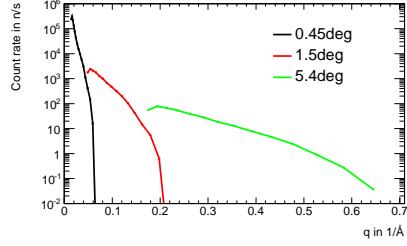
Figure 14: Beam intensity at the sample position as a function of wavelength λ for several angle of incidence θ . The neutron flux depends both on the divergence range, which is $\leq 10\%$ of the incident angle and the footprint size of the 1 cm^2 sample increasing with $\sin \theta$. See also Tab. 2.

454 $q = 0.6 \text{ \AA}^{-1}$ within minutes on a $1 \times 1 \text{ cm}^2$ sample, with at least 100 counts for
 455 every data point. The ability of measuring reflectivities at high q and on sam-
 456 ples of 1 cm^2 size is unprecedented. For example, the FIGARO reflectometer at
 457 ILL is used for measurements up to 0.4 \AA^{-1} with typically much larger sam-
 458 ples.

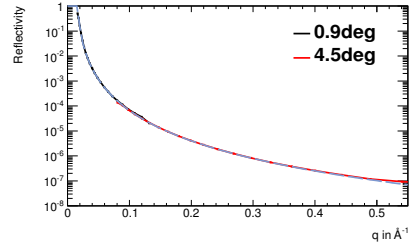
459
 460 It is well known that incoherent background originating from the sample
 461 sets a limit on minimum reflectivity that can still be measured with a certain
 462 statistical significance. For the ideal D_2O surface of $1 \times 1 \text{ cm}^2$ area and 0.3 mm
 463 thickness, the background is of the order of $R_{\text{BG}} = 10^{-6}$ using the mean free
 464 path of $\lambda_i = 7.353 \text{ cm}$ for D_2O for incoherent scattering. Neutronic simulations
 465 with incoherent background included show that even in that case data acqui-
 466 sition times of 100 s suffice in the range up to 0.6 \AA^{-1} , see Fig. 16. Since its
 467 shape is flat, the background can be fitted and subtracted from the reflectivity
 468 spectrum. The residual spectrum agrees well with the theoretical curve and all
 469 data points still have a high enough statistical significance, with 2σ being the
 470 significance of the lowest data point. Thus, if the measurement can be carried
 471 out for a sufficiently long time, being only a few minutes for a $1 \times 1 \text{ cm}^2$ D_2O
 472 sample, reflectivities down to 10^{-7} can be accessed by background recording
 473 and subtraction. In the case of the $1 \times 1 \text{ cm}^2$ monolayer sample, the mean free
 474 path of the null reflecting water is $\lambda_i = 0.202 \text{ cm}$ and yields a background level
 475 of $> 10^{-5}$. For such a sample the total counting time of the order of 4 to 5 hours
 476 (for the largest angular setting) will suffice to achieve a statistically significant



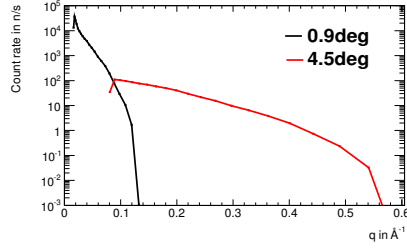
(a) Reflectivity of a D₂O surface measured with the single waveband



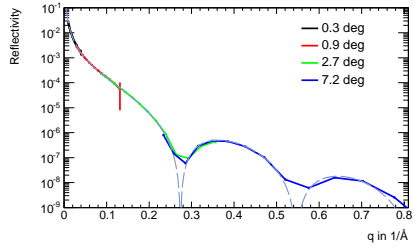
(b) Count rate achieved on a D₂O surface with the single waveband



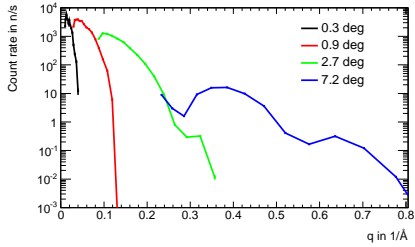
(c) Reflectivity of a D₂O surface measured with the double waveband



(d) Count rate achieved on a D₂O surface with the double waveband



(e) Reflectivity of a Langmuir layer on null reflecting water measured with the single waveband



(f) Count rate achieved on a Langmuir layer on null reflecting water with the single waveband

Figure 15: a) - d): Virtual measurement of an ideal air-D₂O surface with the basic chopper setup and a $d\theta/\theta$ resolution of 10%, using the single waveband and three angular settings and the double waveband and two angular setting, respectively. The count rate at the reflectivity of 10^{-7} is of the order of 1 n/s (0.25 n/s) for the single (double) waveband and thus 100 counts are collected within ≈ 1.5 (6) minutes for the largest angular setting. The ideal reflectivity curve of the D₂O surface is shown in grey for comparison. e) - f): Virtual measurement of a Langmuir layer on null reflecting water reflectivity spectrum with the basic chopper setup and a $d\theta/\theta$ resolution of 10%, using the single waveband and four angular settings. The count rate at the reflectivity of 10^{-8} for the highest reflection angle is of the order of 0.25 n/s, corresponding to a measurement time of 6 minutes for 100 signal counts. The ideal reflectivity curve of the d-DPPE Langmuir layer is shown in grey for comparison. Note that already in the basic setup the thickness of the Langmuir layer can be determined unambiguously, as two adjacent minima positions are resolved.

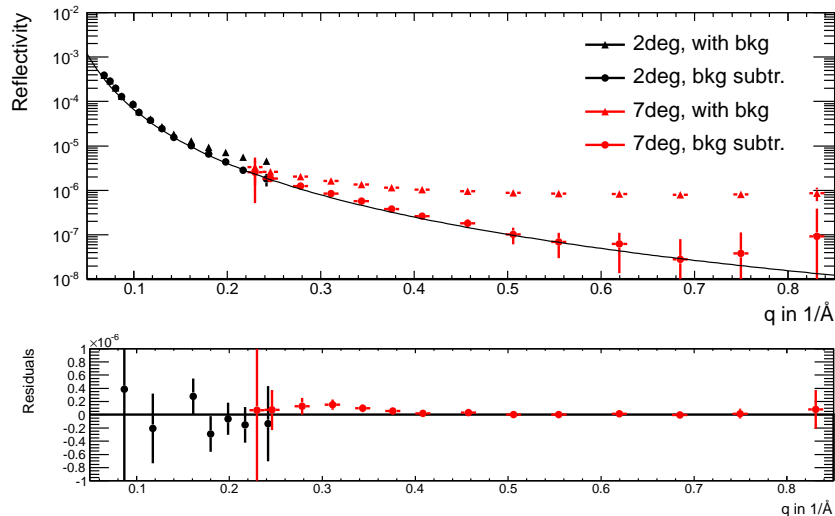


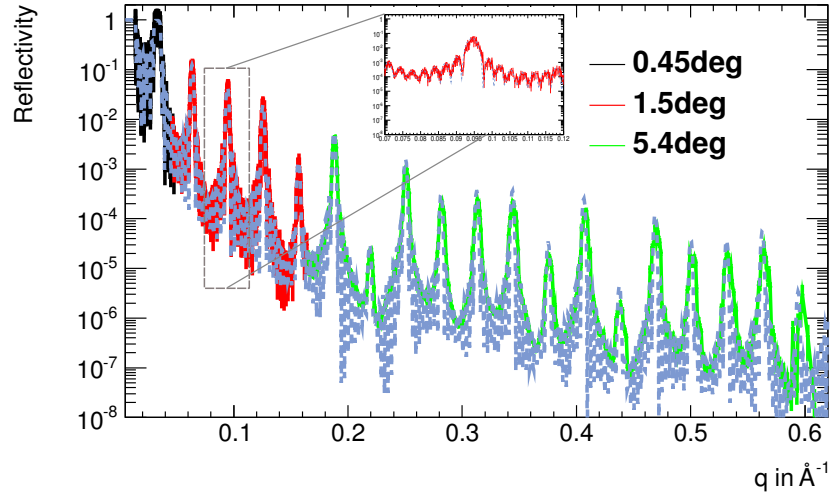
Figure 16: The reflectivity curve of an ideal D₂O surface measured on the reflectometer including background from incoherent scattering. The original curve reaches its minimum at a reflectivity of $\approx 10^{-6}$. After subtracting the flat background (per angular setting) the measurement is in a good agreement with expectations. Note that the error bars correspond to the square root of the number of expected counts collected over 100 s.

477 measurement of the monolayer signal after background subtraction. Naturally,
 478 the required sampling time is inversely proportional to the total sample area
 479 and can be significantly reduced if larger samples (of the order of 10 cm²) are
 480 used.

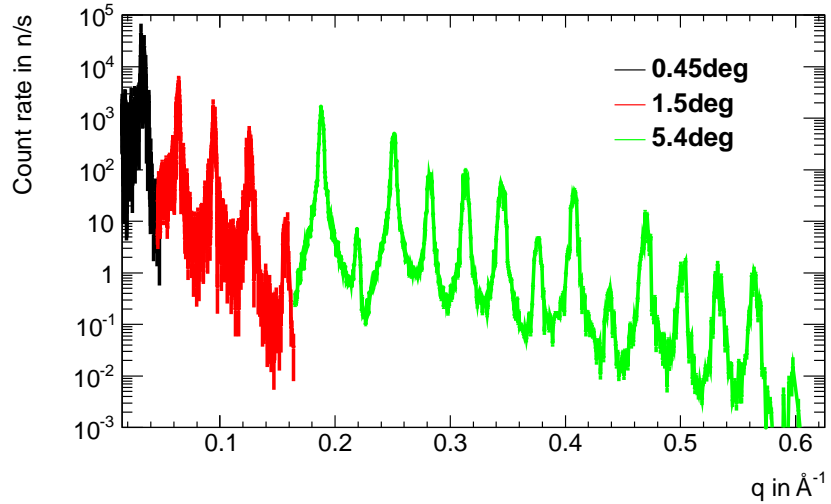
481

482 3.2. High-resolution setup

483 The WFM chopper setup is optimized to provide a constant and high wave-
 484 length resolution for the single waveband from 2 Å to 7.1 Å, combined with
 485 an adequate collimation before the sample for a high q-resolution. Due to a
 486 substantial loss in flux because of increased resolution as compared to the basic
 487 setup, see Fig. 9, the available q-range for such measurements is most likely
 488 reduced to $q < 0.5 \text{ \AA}^{-1}$. Within the accessible q-range, however, fast measure-
 489 ments of highly structured reflectivity spectra are rendered possible. In Fig. 17,
 490 the measurement of a NiTi-multilayer sample ([86 Å Ni/115 Å Ti] on glass, total
 491 thickness = 2010 Å) is shown together with the ideal spectrum of this sample in
 492 grey for comparison. Its reflectivity spectrum exhibits several main peaks along
 493 with Kiessig oscillations over the entire q-range. The high-resolution setup of
 494 the reflectometer proves capable of a precise reconstruction of most of these fea-
 495 tures. To achieve at least 100 counts in each data point, 15 min of acquisition
 496 time for the highest angular setting is needed.



(a) The reflectivity of the NiTi sample



(b) The count rate for the measurement of the NiTi reflectivity

Figure 17: The NiTi reflectivity curve measured on the reflectometer using the high-resolution WFM chopper setup. Even finer structures like Kiessig oscillations in the reflectivity spectrum can be well imaged. The measurement time for this sample would be around 4 min. For the last two angular settings, at least 25 counts per data point (taking into account the lowest count rate of 0.1 n/s) are collected in this way that is sufficient for a statistically significant measurement, if background can be neglected.

Position [m]	Description	Neutron flux [n / s cm ²]
2	Guide entry	7.3×10^{10}
6	End of extraction system	3.6×10^{10}
Basic setup ($\delta\lambda/\lambda = 3\% - 10\%$, $\delta\theta/\theta = 10\%$)		
18.7	Before kink	7.7×10^9
29.9	After kink	6.2×10^9
31	After all choppers	5.7×10^9
44.1	Before bending section	6.3×10^9
52.5	$\theta = 0.3^\circ$	3.1×10^8
	$\theta = 0.45^\circ$	4.8×10^8
	$\theta = 0.9^\circ$	8.3×10^8
	At footprint slit, $\theta = 1.8^\circ$	9.9×10^8
	$\theta = 2.7^\circ$	1.9×10^9
	$\theta = 5.4^\circ$	1.7×10^9
	$\theta = 7.2^\circ$	1.3×10^9
High-resolution setup ($\delta\lambda/\lambda = 2.2\%$, $\delta\theta/\theta = 2.2\%$)		
18.7	Before kink	2.0×10^9
29.9	After kink	1.6×10^9
30.4	After all choppers	1.6×10^9
44.1	Before bending section	1.7×10^9
52.5	$\theta = 0.45^\circ$	3.0×10^7
	At footprint slit, $\theta = 1.5^\circ$	6.0×10^7
	$\theta = 5.4^\circ$	2.3×10^8
High-resolution setup ($\delta\lambda/\lambda = 1\%$, $\delta\theta/\theta = 1\%$)		
18.7	Before kink	1.2×10^9
29.9	After kink	9.4×10^8
30.4	After all choppers	9.1×10^8
44.1	Before bending section	9.9×10^8
52.5	$\theta = 0.45^\circ$	7.5×10^6
	At footprint slit, $\theta = 1.5^\circ$	1.5×10^7
	$\theta = 5.4^\circ$	6.2×10^7

Table 2: Neutron flux at different positions along the instrument for the basic and high-resolution setup, respectively. All values were obtained for the single waveband between 2 Å and 7.1 Å by averaging the flux either over the total guide cross-section at the corresponding position or over a 2×1 cm² rectangle perpendicular to the beam axis for measurements at the footprint slit (Slit 2). The flux at the footprint slit position is influenced both by the number of neutron reflections within the bending section and the opening of the first collimation slit (Slit 1) defining the divergence at the sample position.

497 **4. Concept robustness**

498 The concept of the horizontal reflectometer makes mainly use of established
499 and well known instrument components. The guide system consists of straight
500 sections of 0.5 m. Solely the z-kink piece might require a somewhat smaller seg-
501 mentation. The required coating is $m=5$ for the top and bottom guide surface,
502 while except for the feeding section, the z-kink and the bending section, $m=3$
503 coating can be used everywhere else. The avoidance of the line of sight by the
504 chosen guide geometry is assumed to clear the detector area from background
505 arising from the prompt pulse. Two guide sections were studied more carefully,
506 being the feeding and the deflection sections. The impact of various solutions
507 for the feeding section located in the central monolith was inspected with re-
508 spect to the delivered flux on sample. It was observed that even if the first 2
509 m of the feeding section cannot be installed due to cooling problems or other
510 technical constraints, the flux on a $1 \times 1 \text{ cm}^2$ sample stays without significant
511 changes. Solely for samples with widths larger than 2 cm a drop of intensity
512 occurs. The conclusion is that the instrument does not heavily depend on the
513 actual performance of the extraction system.

514
515 The required stability of the deflecting guide system was studied with re-
516 spect to the flux delivered on the sample. It was found that the misalignment of
517 the individual guide pieces can be as large as 0.01° without causing noticeable
518 flux losses. The precision that is routinely reached today is 0.001° . Thus we
519 conclude that the technical demands for the deflecting section do not pose any
520 risk.

521
522 The chopper system is rather complex, but on the other hand the sizes of the
523 chopper discs and their speed are well within what is technically feasible today.
524 The practical validity of the WFM concept itself was already demonstrated
525 at the BNC reactor in Hungary [57]. Presuming that an adequate detector
526 matching the instrument requirements is provided, the setup for high-resolution
527 measurements does not entail additional risks.

528

529 **5. Discussion and conclusions**

530 The design of the horizontal reflectometer presented in this work has been
531 developed with respect to scientific questions that will be relevant at the time
532 when the ESS facility comes into operation. The horizontal reflectometer proves
533 capable of measurements of high q transfers on small horizontal samples possi-
534 ble within reasonable measurement time, while being very flexible in terms of
535 covered q -range, sample size and beam direction. A dedicated WFM chopper
536 setup for high-resolution measurements on very thick multi-structured samples
537 is currently the first one to be proposed for a reflectometer instrument and its
538 design presented in this work and in [48] shows that the required $\delta q/q$ resolution
539 can be achieved without pushing chopper layouts at or beyond current technical

540 limits. If this setup will be realized at the ESS, areas of parameter space that
541 are currently inaccessible to neutron reflectometry due to limited flux and/or
542 precision are expected to open up for exploration and new insights in materials
543 organization.

544 **Acknowledgements**

545 We thank our colleagues at the ESS for fruitful discussions.
546 This work was funded by the German BMBF under “Mitwirkung der Zentren
547 der Helmholtz Gemeinschaft und der Technischen Universität München an der
548 Design-Update Phase der ESS, Förderkennzeichen 05E10CB1.”

549 **References**

- 550 [1] Bradbury, R.; Penfold, J.; Thomas, R. K.; Tucker, I. M.; Petkov, J. T.;
551 Jones, C., *Langmuir* 2013, 29, (10), 3361-3369.
- 552 [2] Bauer, M.; Fajolles, C.; Charitat, T.; Wacklin, H.; Daillant, J., *Journal of*
553 *Physical Chemistry B* 2011, 115, (51), 15263-15270.
- 554 [3] Yang, B.; Holdaway, J. A.; Edler, K. J., *Langmuir* 2013, 29, (12), 4148-
555 4158.
- 556 [4] Campana, M.; Webster, J. R. P.; Lawrence, M. J.; Zorbakhsh, A., *Soft*
557 *Matter* 2012, 8, (34), 8904-8910.
- 558 [5] Zorbakhsh, A.; Webster, J. R. P.; Wojciechowski, K., *Langmuir* 2009, 25,
559 (19), 11569-11575.
- 560 [6] Dante, S.; Hauss, T.; Steitz, R.; Canale, C.; Dencher, N. A., *Biochimica Et*
561 *Biophysica Acta-Biomembranes* 2011, 1808, (11), 2646-2655.
- 562 [7] Watkins, E. B.; El-Khoury, R. J.; Miller, C. E.; Seaby, B. G.; Majewski, J.;
563 Marques, C. M.; Kuhl, T. L., *Langmuir* 2011, 27, (22), 13618-13628.
- 564 [8] Cardenas, M.; Wacklin, H.; Campbell, R. A.; Nylander, T., *Langmuir* 2011,
565 27, (20), 12506-12514.
- 566 [9] Hellsing, M. S.; Rennie, A. R.; Hughes, A. V., *Langmuir* 2011, 27, (8),
567 4669-4678.
- 568 [10] Tatur, S.; Maccarini, M.; Barker, R.; Nelson, A.; Fragneto, G., *Langmuir*
569 2013, 29 (22), 6606-6614.
- 570 [11] Muller-Buschbaum, P.; Metwalli, E.; Moulin, J. F.; Kudryashov, V.; Haese-
571 Seiller, M.; Kampmann, R., *European Physical Journal-Special Topics*
572 2009, 167, 107-112.
- 573 [12] Bouwman, W. G.; Plomp, J.; De Haan, V. O.; Kraan, W. H.; van Well,
574 A. A.; Habicht, K.; Keller, T.; Rekveldt, M. T., *Nuclear Instruments and*
575 *Methods in Physics Research A*, 2008, 586, (1), 9-14.
- 576 [13] Dalgliesh, R. M.; Langridge, S.; Plomp, J.; de Haan, V. O.; van Well, A.
577 A., *Physica B-Condensed Matter* 2011, 406, (12), 2346-2349.

- 578 [14] Pynn, R.; Ashkar, R.; Stonaha, P.; Washington, A. L., *Physica B-*
579 *Condensed Matter* 2011, 406, (12), 2350-2353.
- 580 [15] Vorobiev, A.; Major, J.; Dosch, H.; Mueller-Buschbaum, P.; Falus, P.;
581 Felcher, G. P.; Velthuis, *Journal of Physical Chemistry B* 2011, 115, (19),
582 5754-5765.
- 583 [16] Griffiths, P. C.; Knight, D. W.; Morgan, I. R.; Ford, A.; Brown, J.; Davies,
584 B.; Heenan, R. K.; King, S. M.; Dalglish, R. M.; Tomkinson, J.; Prescott,
585 S.; Schweins, R.; Paul, A., *Beilstein Journal of Organic Chemistry* 2010, 6,
586 1079-1088.
- 587 [17] Muller-Buschbaum, P., *Polymer Journal* 2013, 45, (1), 34-42.
- 588 [18] Xia, X.; Metwalli, E.; Ruderer, M. A.; Korstgens, V.; Busch, P.; Boni,
589 P.; Muller-Buschbaum, P., *Journal of Physics-Condensed Matter* 2011, 23,
590 (25).
- 591 [19] Parnell, A. J.; Dalglish, R. M.; Jones, R. A. L.; Dunbar, A. D. F., *Applied*
592 *Physics Letters* 2013, 102, (7).
- 593 [20] Ruderer, M. A.; Meier, R.; Porcar, L.; Cubitt, R.; Muller-Buschbaum, P.,
594 *Journal of Physical Chemistry Letters* 2012, 3, (6), 683-688.
- 595 [21] Le Brun, A. P.; Holt, S. A.; Shah, D. S. H.; Majkrzak, C. F.; Lakey, J. H.,
596 *Biomaterials* 2011, 32, (12), 3303-3311.
- 597 [22] Holt, S. A.; Le Brun, A. P.; Majkrzak, C. F.; McGillivray, D. J.; Heinrich,
598 F.; Losche, M.; Lakey, J. H., *Soft Matter* 2009, 5, (13), 2576-2586.
- 599 [23] Huth, M.; Hertrich, S.; Mezo, G.; Madarasz, E.; Nickel, B., *Materials* 2010,
600 3, (11), 4994-5006.
- 601 [24] Yang, B.; Jaber, R.; Edler, K. J., *Langmuir* 2012, 28, (22), 8337-8347.
- 602 [25] 24. Zhuk, A.; Xu, L.; Ankner, J. F.; Sukhishvili, S. A., *Soft Matter* 2013,
603 9, (2), 410-417.
- 604 [26] 25. Pichon, B. P.; Louet, P.; Felix, O.; Drillon, M.; Begin-Colin, S.; Decher,
605 G., *Chemistry of Materials* 2011, 23, (16), 3668-3675.
- 606 [27] Kalisvaart, W. P.; Luber, E. J.; Poirier, E.; Harrower, C. T.; Teichert, A.;
607 Wallacher, D.; Grimm, N.; Steitz, R.; Fritzsche, H.; Mitlin, D., *The Journal*
608 *of Physical Chemistry C* 2012, 116, (9), 5868-5880.
- 609 [28] Jerliu, B.; Dorrer, L.; Huger, E.; Borchardt, G.; Steitz, R.; Geckle, U.;
610 Oberst, V.; Bruns, M.; Schneider, O.; Schmidt, H., *Physical Chemistry*
611 *Chemical Physics* 2013, 15, (20), 7777-7784.
- 612 [29] Brussing, F.; Toperverg, B.; Zhernenkov, K.; Devishvili, A.; Zabel, H.;
613 Wolff, M.; Theis-Brohl, K.; Wiemann, C.; Kaiser, A.; Schneider, C. M.,
614 *Physical Review B* 2012, 85, (17).

- 615 [30] Hjorvarsson, B.; Kudavsov, Y.; Wolff, M.; Hase, T.; Chacon, C.; van Kam-
616 pen, M.; Nordblad, P.; Liebig, A.; Zabel, H., *Epl* 2008, 81, (1).
- 617 [31] Dabkowska, A. P. et al., *Soft Matter* 2013, 9 (29), 7095-7105.
- 618 [32] Wallet, B.; Kharlampieva, E.; Campbell-Proszowska, K.; Kozlovskaya, V.;
619 Malak, S.; Ankner, J. F.; Kaplan, D. L.; Tsukruk, V. V., *Langmuir* 2012,
620 28, (31), 11481-11489.
- 621 [33] Hollinshead, C. M.; Harvey, R. D.; Barlow, D. J.; Webster, J. R. P.; Hughes,
622 A. V.; Weston, A.; Lawrence, M. J., *Langmuir* 2009, 25, (7), 4070-4077.
- 623 [34] Bauer, M.; Bernhardt, M.; Charitat, T.; Kekicheff, P.; Fajolles, C.; Frag-
624 neto, G.; Marques, C. M.; Dailant, J., *Soft Matter* 2013, 9, (5), 1700-1710.
- 625 [35] Eastman, S. A.; Kim, S.; Page, K. A.; Rowe, B. W.; Kong, S. H.; Soles, C.
626 L., *Macromolecules* 2012, 45, (19), 7920-7930.
- 627 [36] Leitch, J. J.; Collins, J.; Friedrich, A. K.; Stimming, U.; Dutcher, J. R.;
628 Lipkowski, J., *Langmuir* 2012, 28, (5), 2455-2464.
- 629 [37] Strobl, M.; Steitz, R.; Kreuzer, M.; Rose, M.; Herrlich, H.; Mezei, F.;
630 Grunze, M.; Dahint, R., *Review of Scientific Instruments* 2011, 82, (5),
631 055101-9.
- 632 [38] Kreuzer, M.; Strobl, M.; Reinhardt, M.; Hemmer, M. C.; Hau, T.; Dahint,
633 R.; Steitz, R., *Biochimica et Biophysica Acta (BBA) - Biomembranes* 2012,
634 1818, (11), 2648-2659.
- 635 [39] Ioffe, A.; Babcock, E.; Pipich, V.; Radulescu, A., *JCNS Workshop on*
636 *Modern Trends in Production and Applications of Polarized 3HE*, Babcock,
637 E.; Gutberlet, T.; Ioffe, A., Eds. 2011; Vol. 294.
- 638 [40] European Spallation Source, URL <http://www.esss.se>
- 639 [41] Wolff, M.; Steitz, R.; Gutfreund, P.; Voss, N.; Gerth, S.; Walz, M.; Magerl,
640 A.; Zabel, H., *Langmuir* 2008, 24, (20), 11331-11333.
- 641 [42] Gutfreund, P.; Wolff, M.; Maccarini, M.; Gerth, S.; Ankner, J. F.; Brown-
642 ing, J.; Halbert, C. E.; Wacklin, H.; Zabel, H., *Journal of Chemical Physics*
643 2011, 134, (6), 064711.
- 644 [43] Kampmann, R.; Haese-Seiller, M.; Kudryashov, V.; Nickel, B.; Daniel, C.;
645 Fenzl, W.; Schreyer, A.; Sackmann, E.; Radler, J. *Physica B-Condensed*
646 *Matter* 2006, 385-86, 1161-1163
- 647 [44] K. Lieutenant et al., *Proc. SPIE* 5536(1) (2004) 134-145
- 648 [45] K. Lefmann and K. Nielsen, *Neutron News* 10/3 (1999) 20
- 649 [46] K. Klenø et al., *Nuclear Instruments and Methods in Physics Research A*
650 696 (2012) 75-84

- 651 [47] L. D. Cussen et al., Nuclear Instruments and Methods in Physics Research
652 A 705 (2013) 121-131
- 653 [48] D. Nekrassov et al., Nuclear Instruments and Methods in Physics Research
654 A (2013), DOI 10.1016/j.nima.2013.03.001
- 655 [49] M. Strobl et al., Nuclear Instruments and Methods in Physics Research A
656 705 (2013) 74-84
- 657 [50] Felcher, G. P.; Velthuis, S. G. E. t.; Major, J.; Dosch, H.; Anderson, C.;
658 Habicht, K.; Keller, T., Advances in Neutron Scattering Instrumentation,
659 SPIE, 2002, 4785, 164-173.
- 660 [51] Major, J.; Dosch, H.; Felcher, G. P.; Habicht, K.; Keller, T.; te Velthuis, S.
661 G. E.; Vorobiev, A.; Wahl, M., Physica B: Condensed Matter, Proceedings
662 of the Seventh International Conference on Surface X-ray and Neutron
663 Scattering, 2003, 336, 8-15.
- 664 [52] Ashkar, R.; Stonaha, P.; Washington, A. L.; Shah, V. R.; Fitzsimmons, M.
665 R.; Maranville, B.; Majkrzak, C. F.; Lee, W. T.; Schaich, W. L.; Pynn, R.;
666 J. Appl. Cryst., International Union of Crystallography, 2010, 43, 455-465.
- 667 [53] Ashkar, R.; Schaich, W. L.; de Haan, V. O.; van Well, A. A.; Dalglish, R.;
668 Plomp, J.; Pynn, R., J. Appl. Phys., 2011, 110, 102201-6.
- 669 [54] Miller, C. E., et al., Biophysical Journal 2008, 95 (2), 629-640
- 670 [55] Pabst, G., et al., Physical Review E 2000, 62 (3), 4000-4009
- 671 [56] Wydro, P., et al., Biochimica Et Biophysica Acta-Biomembranes 2012, 1818
672 (7), 1745-1754
- 673 [57] M. Russina et al., Nuclear Instruments and Methods in Physics Research
674 A 654 (2011) 383-389